



**HAL**  
open science

**Mesoscopic structure of dry-pressed clay samples from  
small-angle X-ray scattering measurements . In :  
Proceedings of the XIIIth International Conference on  
Small-Angle Scattering**

Yves Méheust, Simon Dagois-Bohy, Kenneth Knudsen, Jon Fossum

► **To cite this version:**

Yves Méheust, Simon Dagois-Bohy, Kenneth Knudsen, Jon Fossum. Mesoscopic structure of dry-pressed clay samples from small-angle X-ray scattering measurements . In : Proceedings of the XIIIth International Conference on Small-Angle Scattering. Journal of Applied Crystallography, 2007, 40 (s1), pp.s286-s291. 10.1107/S0021889807008552 . insu-00177120

**HAL Id: insu-00177120**

**<https://insu.hal.science/insu-00177120>**

Submitted on 5 Oct 2007

**HAL** is a multi-disciplinary open access archive for the deposit and dissemination of scientific research documents, whether they are published or not. The documents may come from teaching and research institutions in France or abroad, or from public or private research centers.

L'archive ouverte pluridisciplinaire **HAL**, est destinée au dépôt et à la diffusion de documents scientifiques de niveau recherche, publiés ou non, émanant des établissements d'enseignement et de recherche français ou étrangers, des laboratoires publics ou privés.

# Mesoscopic structure of dry-pressed clay samples from small-angle X-ray scattering measurements

Yves Méheust,<sup>a,c\*</sup> Simon Dagois-Bohy,<sup>a</sup> Kenneth D. Knudsen<sup>b</sup> and Jon O. Fossum<sup>a\*</sup>

<sup>a</sup>Physics Department, Norwegian University of Science and Technology (NTNU), Norway, <sup>b</sup>Physics Department, Institute for Energy Technology (IFE), Kjeller, Norway, <sup>c</sup>Geosciences Rennes, UMR CNRS 6118, Université Rennes 1, Rennes, France.  
E-mail: yves.meheust@univ-rennes1.fr, jon.fossum@ntnu.no

We study weakly-hydrated samples of platelet-shaped nanoparticles obtained by dry-pressing suspensions of the synthetic Na-fluorohectorite clay. The particles consist of stacks of several tenths of 1 nm-thick nanosilicate sheets. They form a compound of quasi-two-dimensional particles whose average director is aligned with the direction of the uniaxial stress applied at dehydration. Small-angle X-ray scattering images from these samples are either isotropic or anisotropic, depending on the sample orientation with respect to the X-ray beam. From anisotropic images, we investigate changes in the scattering objects' orientation distribution probability (ODP) function, as we lower the temperature, thus triggering swelling of the individual particles by water intercalation. This is done on the one hand by inferring the width of the ODP function from the eccentricity of quasi-elliptic iso-intensity cuts of the small-angle scattering images, and on the other hand by obtaining the ODP function from azimuthal profiles of the images. The decays of the scattering intensity as a function of momentum transfer along the two principal directions of the images exhibit power law behaviors. A crossover scale between two power law regimes is observed on the profiles recorded along the horizontal axis; it corresponds to the typical pore size along the direction of the initially-applied load. These results are compared to a previous study of similar systems.

## 1. Introduction

Clays are minerals with a grain size smaller than 2  $\mu\text{m}$ . From the morphological point of view, they consist of platelet-shaped grains/crystallites (Velde, 1992). The basic structural unit of 2:1 clays, in particular, is a 1 nm-thick phyllosilicate platelet with a negative structural charge on the top and bottom surfaces. Such is Laponite, a much-studied model system for monodisperse platelet colloids (Mourchid *et al.*, 1998; Bonn *et al.*, 1999; Lemaire *et al.*, 1996). Another synthetic 2:1 clay is fluorohectorite. It possesses a structural charge much larger than that of laponite (1.2  $e^-$  as opposed to 0.4  $e^-$ ), which allows the platelets to stack by sharing an intercalated cation X (the particular clay being denoted as X-fluorohectorite) and to remain stacked either in dispersed- or weakly-hydrated state. In poly-crystalline fluorohectorite samples, the grains therefore consist of such nano-stacked particles, with a thickness of about 100 nm (DiMasi *et al.*, 2001; da Silva *et al.*, 2002). They remain platelet-shaped and essentially two-dimensional, their lateral dimension being much larger than their thickness. They also exhibit a large polydispersity in their lateral sizes.

Weakly-hydrated assemblies of nano-stacked particles can be studied in the framework of intercalation compounds (Solin, 1993). Hydration of individual clay particles, in particular, occurs through the

intercalation of water molecules in the space between adjacent silica platelets, inside the stacks. The stepwise swelling of the nano-stacks resulting from molecular packing between clay platelets (Skipper *et al.*, 1991; Skipper *et al.*, 1991), is a well-known first order transition between hydration states corresponding to up to 4 (Suzuki *et al.*, 1987; Wada *et al.*, 1990; da Silva *et al.*, 2002). "water layers". The thermodynamically stable state is controlled by the ambient temperature ( $T$ ) and humidity ( $H$ ), and transitions occurring along given ( $H, T$ ) lines (Wada *et al.*, 1990; da Silva *et al.*, 2003). For Na-Fluorohectorite and at  $H \simeq 100\%$ , for example, the system goes from 0 water layers (WL) up to 2WL between 393 and 275 K (da Silva *et al.*, 2003).

In this paper, we study weakly-hydrated poly-crystalline samples of Na-fluorohectorite obtained by dry-pressing aqueous suspensions, under a uniaxial load. In such samples, the platelet-shaped nano-stacks are tightly packed and preferentially oriented perpendicular to the load applied at dehydration. Re-hydrating them causes particle-swelling, and a subsequent re-arrangement of the particles with respect to each other. In a recent study (Méheust *et al.*, 2006a), we studied similar samples and monitored the changes in the particles' orientation probability densities during hydration transitions. In this paper, we also investigate the changes in the geometry of the whole weakly-hydrated assembly under the effect of individual particle swelling, but using small-angle X-ray scattering (SAXS), thus probing larger length scales. Note that small-angle neutron scattering (SANS) has previously been used on similar samples, focusing on typical pore sizes (Knudsen *et al.*, 2004). Here we address predominantly orientational order.

## 2. Theoretical background

### 2.1. Sample geometry

The meso-structure of the samples consists of an assembly of Na-fluorohectorite particles, i. e., of  $\sim 100$  nm-thick platelet-shaped nano-stacks. The orientation of one clay particle can be described through its director, a unit length director  $\mathbf{n}$  normal to the top/bottom surfaces of the particle.

The collective geometry of these particles retains a trace of the compaction process that created it: the particles have their directors on average parallel to the direction of the load applied during dehydration. We denote that direction by a mean director  $\mathbf{n}_0$ . In Fig. 1, we show a schematical cut of a sample through a plane parallel to  $\mathbf{n}_0$ . The directors of the various particles are distributed in the entire solid angle according to an orientation distribution probability function  $f$  that only depends on the deviation angle  $\alpha$  of a given director from the mean director  $\mathbf{n}_0$  (Méheust *et al.*, 2006a). This geometric description is identical to that of a uniaxial nematic liquid crystal. In order to describe the shape of the ODP function, we use a function identical to that obtained by Maier and Saupe in their classical description of the uniaxial nematic order (Maier & Saupe, 1958; Maier & Saupe, 1959), in the form

$$f(\alpha) \propto \exp(m \cos^2 \alpha) . \quad (1)$$

Note that: (i)  $f$  is normalized to 1 on the range  $\alpha \in [0; \pi/2]$ , (ii)  $m$  is a parameter that controls the width of the distribution, and (iii) in contrast to nematic liquid crystals, there is no theoretical reason to motivate the choice of that particular function in our system. In the process of fitting a model to the data in order to quantify the angular width of the distribution, the Maier-Saupe function provided good fits while allow-

ing to relate our observations to a well-known description of an analog geometry.

Regarding the shape of the distribution, the parameter  $m$  controls the angular width of the distribution. We rather characterize the half-width as the two-dimensional (2D) root mean square of the distribution, defined as

$$\sqrt{\langle \alpha^2 \rangle_f} = \left( 2\pi \int_0^{\pi/2} \alpha^2 f(\alpha) \sin \alpha d\alpha \right)^{1/2}. \quad (2)$$

To a first approximation, the porous space inside the samples can be described as a system with a mesoporosity at the  $0.1 - 1 \mu\text{m}$  scale, in-between the clay particles (see gray shading in Fig. 1), and a microporosity in the inter-layer spaces of the clay particles, i. e., in-between adjacent platelets inside the nano-stacks (see red lines in Fig. 1).

## 2.2. Small-angle scattering by aggregates of particles

Small angle scattering profiles recorded from aggregates of colloids often exhibit power laws on a wide  $q$  range (Dietler *et al.*, 1986; Schaefer & Keefer, 1986; Vacher *et al.*, 1988). Except for the anisotropy of the platelet-shaped clay particles and the overall orientational order of their assembly, these models are well suited to describe scattering by the samples presented in section 2.1. Power laws in the scattering curves arise from long range correlations either in the mass geometry of the aggregates, or in the roughness of their pores. However, the exponent  $D$  of the power law

$$I(q) = A q^{-D} + B \quad (3)$$

( $B$  is the incoherent background scattering) that is fitted to the scattering data is related to the fractal property of the scattering aggregate in a way that depends on whether one addresses a mass- or a surface-fractal (Schmidt, 1989):

If we consider systems in which the aggregated particles are positioned with respect to one another so that their two-point correlation function is a power law function in the form

$$g(r) \propto r^{D_m-3}, \quad (4)$$

where  $D_m$  is a fractal dimension, a power law scattering curve with an exponent  $-D_m$  is observed for  $q$  values in the range  $1/l \ll q \ll 1/a$ . Here  $a$  is the typical size of an aggregated particle, and  $l$  is the size of the whole system, i.e., the largest accessible length scale (Sinha *et al.*, 1984; Schmidt, 1989). The exponent  $D$  in Eq. (3) is simply  $D = D_m$ , and is by definition in the range  $1 \leq D < 3$ .

If we now probe length scales smaller than the particle size, the scattering becomes sensitive to the roughness of the aggregated particles. If this roughness qualifies the particle for being considered a surface fractal with a dimension  $D_s$ , or more generally if the area of the surface is a power law of its linear dimension with an exponent  $D_s$  on a given range of scales, then the scattering profiles exhibit a power law behavior with an exponent  $-(6 - D_s)$  on that range of scales (Bale & Schmidt, 1984; Schmidt, 1989). Here by definition  $D_s$  is in the range  $2 \leq D_s < 3$ , and the exponent  $D$  in the range  $3 < D \leq 4$ , with the well-known Porod law limit (4) being reached for smooth particles (Porod, 1951).

Therefore, the scattering curve can be interpreted as resulting either from surface scattering, or from bulk scattering, depending on whether the exponent is in the range  $3 < D \leq 4$  or in the range  $1 \leq D < 3$ . Often those two behaviors are both present, on two  $q$  ranges corresponding to length scales smaller- or larger- than the typical particle size, respectively. Note that the understanding of such data is more difficult in the presence of a polydispersity of the aggregated particles, or,

equivalently, of a wide distribution for the pore sizes. In this case, an exponent  $D > 3$  can arise both from surface scattering from rough pore walls, or from bulk scattering by a porous media with a wide pore size distribution (Pfeifer & Avnir, 83). In the case of the anisotropic clay particles, which have two characteristic length scales instead of one, the experiments are carried out in an intermediate  $q$  range corresponding to length scales intermediate between the typical particle thickness and the typical particle width.

## 2.3. Orientation distribution probability functions of platelet-shaped scattering objects from two-dimensional SAXS data

If the incoming X-ray beam hits the sample perpendicular to the mean platelet director  $\mathbf{n}_0$  (direction (2) in Fig. 1), the preferential orientation of the scattering objects results in an anisotropy of the two-dimensional small-angle scattering images. For nematic systems of monodisperse platelets, the ODP function can be computed from small-angle data, provided that there is no coupling between positional and orientational order, or that no positional correlations are found in the probed  $q$  range. Indeed, under these assumptions, the scattering intensity is proportional to the integral over the ODP function of the form factor  $F(\mathbf{q})$  of an individual platelet-shaped particle:

$$I(q, \phi) \propto \int f(\alpha) F(\mathbf{q}) \sin \alpha d\alpha. \quad (5)$$

Using this relation, Lemaire *et al.* have fitted a model to the whole two-dimensional scattering pattern in order to compute the order parameter of a nematic dispersion of laponite colloids (Lemaire *et al.*, 1996). Note that Eq. (5) still holds when a polydispersity is present, but a further integration on the varying size parameter(s) must be included.

Recently, van der Beek *et al.* proposed a method to infer the ODPs function based on the monitoring of the scattering intensity along circular rings (at a given  $q$  value), for systems in which Eq. (5) is valid (van der Beek *et al.*, 2006). The authors derived an expression for the scattering intensity in the range of  $q$  values corresponding to length scales intermediate between the platelet thickness and the platelet width, in the form

$$I(q, \phi) \propto \frac{f(\alpha = \phi)}{q^2}, \quad (6)$$

where  $\phi$  is the azimuthal angle. Their study was carried out on a suspension of Gibbsite colloids that were partially aligned by an external magnetic field, and consequently had their directors uniformly distributed in a plane orthogonal to the magnetic field. Such a configuration is analog to, but different from, the nematic geometry addressed here. However, a closer look at the details of their method shows that it can be applied to a configuration such as that presented in Fig. 1, with the beam arriving at the sample according to direction (2).

In our polydisperse system, the exponents of  $q$ -plots is significantly different from  $-2$  (see section 2.2). Nevertheless, we assume to a first approximation that we can consider, as in the monodisperse case, that the azimuthal intensity variations are controlled by the ODP function and decoupled from the decay along the (radial)  $q$ -axis. Hence, we assume that

$$I(q, \phi) \propto \frac{f(\alpha = \phi)}{q^\gamma}, \quad (7)$$

in which  $\gamma$  is an average decay exponent for our system. In what follows, we use Eq. (7) to infer the ODP function from two-dimensional SAXS data.

## 3. Experiments

### 3.1. Experimental method:

**3.1.1. Samples:** Suspension samples were prepared from sodium fluorohectorite produced by Corning Inc., New York. The raw powder was first suspended in deionized water and stirred for several days. The suspensions were then ion-exchanged in solutions of NaCl, for two days and with an excess of Na<sup>+</sup> cations approximately 5 times the cation exchange capacity (Kaviratna *et al.*, 1996), so as to yield a suspension where the cations intercalated inside the colloids are all Na<sup>+</sup>. After removal of the supernatant and of excess cations, by dialysis, the suspension samples were heat-pressed at a temperature of 120°C, applying a moderate uniaxial load (0.12 MPa) in the direction of gravity. The resulting dehydrated samples were disks with a diameter of 7.2 cm and a thickness of ~ 2 mm. The global porosity of the samples (i.e. ratio of the pore volume to the total volume) was measured to be 50 % (Knudsen *et al.*, 2004). The clay disks were then cut into 2 × 2 × 6 mm<sup>3</sup> parallelepipedic slices, proper for synchrotron experiments.

**3.1.2. SAXS experiments:** Measurements were carried out at beamline BM-26B of the European Synchrotron Radiation Facility (ESRF), in Grenoble (France), using an energy ~ 8 keV. Scattered X-rays were recorded on a 2-dimensional detector (a square matrix of 512 × 512 elements). The X-ray wavelength and the camera length were both calibrated using the fiber diffraction of wet rat-tail collagen, which has strong characteristic peaks at  $q = 2\pi n/67.2 \text{ nm}^{-1}$  ( $n = 1, 3, 5$ ). The wavelength was found to be  $\lambda = 1.53 \text{ \AA}$  and the camera length  $D = 8355 \text{ mm}$ . The exposure time for each image was 500 s. This wavelength and this camera length, combined with the diameters of the detector and beam stop, provided SAXS data in a range of momentum transfer values between  $q_{\min} = 0.02 \text{ nm}^{-1}$  and  $q_{\max} = 0.31 \text{ nm}^{-1}$ .

The samples were placed in a custom-made cell that ensured control of the temperature and relative humidity in the vicinity of the sample. A detailed description of this cell can be found in (Méheust *et al.*, 2006a). Two orthogonal orientations of the sample with respect to the incoming X-ray beam were used; they are denoted (1) and (2) in Fig. 1. The sample thickness parallel to the incoming beam was 2 mm, in both configurations.

**3.1.3. Protocol:** After distance calibrations and proper sample positioning, we performed a series of measurements in configuration (1) (see Fig. 1) under large relative humidity ( $H = 98\%$ ), decreasing temperatures between 393 K and 278 K, in steps of 30 to 10 K. The hydration state at the beginning of the series was a mix of 0WL and 1WL states; at the end of the series it was a 2WL state. After imposing each new temperature value, 6 SAXS pictures were taken regularly during 1h. In what follows, we only present the results obtained from the last picture at a given temperature. We assume that for this picture, the system had time to adjust to the imposed temperature, in particular with respect to water intake.

Subsequently, the sample was rotated into configuration (2) (see Fig. 1), and the same series of measurements was performed again.

### 3.2. Results

**3.2.1. Anisotropy of the SAXS images:** Fig. 2 shows two SAXS images recorded at 333 K, in configurations (1) and (2). In configuration (1), the image is isotropic, which is expected due to the axial symmetry (at least statistically) of the sample meso-structure around the average director  $\mathbf{n}_0$ . An anisotropy could be observed if this director's direction were significantly different from that of the incident beam, which does not seem to be the case. In contrast, the image obtained from configuration (2) is strongly anisotropic; it is this type of images that are to be analyzed to infer the ODP functions of the clay particles

in the sample.

An estimate of the image anisotropy was obtained by fitting ellipses to iso-intensity lines of the images. In practice, a narrow intensity range was considered, in order to improve the statistics. The fits provided the ellipse large semi-axis,  $a$ , its short semi-axis,  $b$ , and their directions. The eccentricity  $e = \sqrt{1 - b^2/a^2}$  was computed and used to quantify the image anisotropy. For perfectly random orientations of the particles, the ellipse is a circle and  $e = 0$ ; for a system of perfectly aligned platelets, the eccentricity is expected to approach 1. A systematic check of the influence on the elliptic fit parameters of the intensity level chosen to perform the fit provided an uncertainty on  $e$  of  $\pm 0.01$ , while the uncertainty on the direction of the axes was found to be  $\sim \pm 1^\circ$ . The evolution of the eccentricity when decreasing temperature is addressed in section 3.2.2.

Radial intensity profiles were then extracted along the principal directions of the image, as defined by the ellipse orientation; they were obtained by integrating sectors of the image,  $\pm 5^\circ$ -wide and centered on those directions, over azimuthal angles. The two profiles obtained from the image shown in Fig. 2(2) are presented in Fig. 3. They are different from each other in that the horizontal profile, denoted (a), exhibits a crossover at a length scale  $q_c = 0.071 \text{ nm}^{-1}$  corresponding to a length scale  $l_c = 1/q_c \sim 14 \text{ nm}$ . This length should be attributed to a typical pore size in the direction of the applied pressure. Particles present, on average, their lateral side to the beam, with their thickness along the horizontal direction; consequently, the pores resulting from particle aggregation exhibit a large aspect ratio: their smallest dimension is found along that direction (Knudsen *et al.*, 2004). The average thickness typical of these clay particles in suspension (around 100 nm) is itself out of our data range. Note that the typical pore size (which is further discussed in section 4) should not be understood in terms of a repeated motif in the meso-structure, since we do not observe a correlation peak at this length scale; it is not allowed by the system's disorder (arising mostly from the particle polydispersity). At length scales smaller than  $l_c$ , the exponent of the power law (Eq. (3)) is  $D = 4$  which indicates scattering by smooth surfaces; at length scales larger than  $l_c$ , the exponent is larger than-, but close to  $D = 3$ , indicating surface scattering by very rough surfaces.

Along the vertical direction, in contrast, a single power law is observed with an exponent intermediate between the two latter regimes. Indeed, if a typical length scale exists along that direction (i.e. a mean particle length or equivalently a mean vertical pore size), it is larger than the larger scale probed by the SAXS ( $\sim 200 \text{ nm}$ ). Note that in the scale range addressed by the SAXS experiment, the particle surfaces are rougher along the vertical direction than horizontally. This difference in the exponent is not surprising, as the horizontal roughness as probed by the SAXS arises mostly from the stacking of the individual platelets into a clay particle, while the vertical roughness (i. e., along a particle's edge), is related to the irregular shape of individual platelets, in the form of an irregular polygon.

This radial behavior has been observed on several different images, but its dependence on temperature has not been investigated yet.

**3.2.2. ODP widths from the eccentricity values** Assuming the validity of Eq. (7), it is possible to relate the eccentricity of the iso-intensity lines to the width of the ODP function. Following the line of page 54 in chapter 4 of (van der Beek, 2005), which dealt with a monodisperse system, the ratio  $f(\phi)/q^\gamma$  is constant along such a line, and therefore, since the semi-axes  $a$  and  $b$  of the ellipse are given in terms of  $q$  values, the ratio of the minimal value of the ODP function

along the line,  $f_{\min}$ , to that of its maximal value,  $f_{\max}$  can be written as

$$\frac{f_{\min}}{f_{\max}} = \left(\frac{b}{a}\right)^{\gamma} = (1 - e^2)^{\frac{\gamma}{2}}. \quad (8)$$

Introducing the form chosen for the ODP function, one obtains the  $m$  parameter from the eccentricity as

$$m = -\frac{\gamma}{2} \ln(1 - e^2). \quad (9)$$

The two-dimensional RMS width of the distribution is then computed numerically.

In Fig. 5(a), we show in red, and with error bars, the eccentricity values as a function of the decreasing temperature. We have used an intensity value corresponding to  $q$  values smaller than  $q_c$ . The ODP widths inferred from these eccentricities are shown in blue, with error bars as well; they were computed using  $\gamma = -3.2$ , a value that we obtained from Fig. 3, as an average of the exponents in plots (a) (value  $-3.1$ ) and (b) (value  $-3.3$ ) at  $q$  values smaller than  $q_c$ .

**3.2.3. ODPs from azimuthal intensity profiles:** Azimuthal profiles extracted at the same  $q$  value ( $0.045 \text{ nm}^{-1}$ ), in the intermediate  $q$  regime, are plotted for all temperatures in Fig. 4. The plots have been normalized to 1 on the  $[0; 2\pi]$   $\phi$  range, and subsequently translated vertically, for clarity. Maier-Saupe functions in the form of Eq. (1) have been fitted to them; they are shown on top of the experimental data. Their 2D RMS width is plotted in blue in Fig. 5(b), as a function of temperature.

The width of the ODP function, whether inferred from eccentricity values (Fig. 5(a)) or from azimuthal profiles (Fig. 5(b)), increases below 313 K, by a value that appears small but is significant with respect to the uncertainty on the fit parameter  $m$ . This behavior indicates a decrease in the orientational order of the scattering objects as clay particles swell by water intercalation.

## 4. Discussion

In a previous study, we addressed the same topic from two-dimensional wide-angle scattering (WAXS) data. The ODP functions for similar samples were inferred from the azimuthal dependence of the amplitude of diffraction peaks, following a method that we have recently developed (Méheust *et al.*, 2006b). We observed an increase in the orientational order during the hydration transitions (Méheust *et al.*, 2006a), which we attributed to steric effects: during sample preparation, the platelet-shaped particles do not have time to find the most favorable configuration; they are locked into a more ordered meso-structure by the constraint arising from the swelling of the individual particles. The 2D RMS width of the ODPs computed in (Méheust *et al.*, 2006a) were around  $40$  to  $50^\circ$  (see also the rocking curve in (da Silva *et al.*, 2002)). The two studies seem to be in contradiction when it comes to whether ordering increases or decreases as a consequence of particle swelling. Though different samples were addressed in the two studies (the load applied at dehydration are respectively  $0.12 \text{ MPa}$  and  $2.60 \text{ MPa}$ ), this apparent discrepancy is probably not so much due to the difference in the sample preparation, but stems from the fact that the objects probed by WAXS and SAXS are different. Indeed, the ODPs obtained from WAXS are those of the thick ( $\sim 100 \text{ nm}$ ) nano-stacked particles (Méheust *et al.*, 2006b), which are rather well aligned; clay particles belonging to the lower tail of the thickness distribution do not contribute to the WAXS signal. In contrast, the exponents measured radially on the SAXS images (Fig. 3) indicate surface scattering from discontinuities in the porous medium consisting of the aggregated clay particles: SAXS is sensitive to all discontinuity surfaces, not only those

belonging to thick nano-stacked particles. The ODPs inferred from the SAXS signal are therefore relative to diffracting objects that are considerably different from-, and less ordered in their orientation than-, the nano-stacked particles probed by WAXS. Considering that the discontinuity surfaces at which scattering properties vary the most are those between a clay particles and an adjacent cavity, and invoking the Babinet principle, we may argue that the SAXS signal can be partly interpreted from the population of cavities/pores, which is complementary to the clay aggregate and is also expected to consist of anisotropically-shaped objects. This is supported by the crossover length scale at  $14 \text{ nm}$ , which we interpret as a typical pore size in the direction parallel to the initially-applied load. Apparently, the ordering of the population of cavities decreases at hydration, while that of the thick nano-stacks increases. Both effects are detectable but quite limited, though, and one might argue that there is hardly no change in the assembly's ordering due to the effect of individual particle swelling.

Note also that the ODP width plots shown in Fig. 5(a) and Fig. 5(b), though qualitatively similar, do not superimpose. Width values inferred from ellipse eccentricities are overestimated with respect to those obtained from monitoring the scattering intensity at a fixed  $q$  value. This shows the limits of this simple analysis, in which we have adapted to a polydisperse system a theory initially developed for a monodisperse system. However, we believe that this study still grabs the qualitative change of orientational order within the clay assembly.

## 5. Conclusion

Two-dimensional SAXS data was used to quantify the orientational order in dry-pressed samples of platelet-shaped clay particles. The temperature was changed in order to trigger hydration transitions and consequently particle swelling, and changes in ODP functions were monitored. The method seems to be able to detect very small changes in the ODPs width. By comparison with a previous study that provided clay particle ODP functions from WAXS data, we conclude that the ODP functions probed by SAXS are relative to all discontinuity surfaces in the clay aggregate, at the probed scales, and are therefore quite different from those obtained from WAXS data.

The prospects to this study are many. The first one is to extend the experiments, both of hydration and dehydration, and to investigate the dependence of  $q$  plots such as those shown in Fig. 3 on temperature. An interesting study would also consist in a joint use of WAXS and SAXS to estimate ODPs in such samples, confronting the two techniques. This could be done on samples with various overall densities (going from gels to pressed samples), so as to characterize if (and when) the observed SAXS data converges to that of individual platelets (Eq. (5)) when the density is increased: the ODPs obtained from SAXS are then expected to converge to those obtained from WAXS. Finally, one could think of improving the method used here so as to account for the direction of the incident beam not being perfectly parallel to that of the average particle director, which results in the amplitudes of the two peaks in Fig. 4 being different.

We acknowledge the help of Igor Dolbnya at the DUBBLE beamline (ESRF) for alignment of the X-ray optics and trouble-shooting with the acquisition setup. This work was supported by the Research Council of Norway (RCN) through a Strategic University Program and through the Nanomat Program: RCN projects 152426/431, 154059/420, 148865/432, and 138368/V30 and SUP154059/420. We also thank the two anonymous referees for their suggestions.

References

Bale, H. D. & Schmidt, P. W. (1984). *Phys. Rev. Lett.* **53**, 596.  
 van der Beek, D. (2005). *Liquid crystal phase behavior of colloidal platelets in external fields*. Ph.D. thesis, Utrecht University.  
 van der Beek, D., Petukhov, A. V., Davidson, P., Ferré, J., Jamet, J. P., Wensink, H. H., Vroege, G. J., Bras, W. & Lekkerkerker, H. N. W. (2006). *Phys. Rev. E*, **73**, 041402.  
 Bonn, D., Kellay, H., Tanaka, H., Wegdam, G. & Meunier, J. (1999). *Langmuir*, **15**, 7534–7536.  
 da Silva, G. J., Fossum, J. O., DiMasi, E., Måløy, K. J. & Lutnæs, S. B. (2002). *Phys. Rev. E*, **66**(1), 011303.  
 Dietler, G., Aubert, C. & Cannell, D. S. (1986). *Phys. Rev. Lett.* **57**, 3117.  
 DiMasi, E., Fossum, J. O., Gog, T. & Venkataraman, C. (2001). *Phys. Rev. E*, **64**, 061704.  
 Kaviratna, P. D., Pinnavaia, T. J. & Schroeder, P. A. (1996). *J. Phys. Chem. Solids*, **57**, 1897.  
 Knudsen, K. D., Fossum, J. O., Helgesen, G. & Haakestad, M. W. (2004). *Physica B*, **352**(1-4), 247–258.  
 Lemaire, B. J., Panine, P., Gabriel, J. C. P. & Davidson, P. (1996). *Europhys. Lett.* **59**, 55–61.  
 Maier, W. & Saupe, A. (1958). *Naturforsch. Z.* **A13**, 564.  
 Maier, W. & Saupe, A. (1959). *Naturforsch. Z.* **A14**, 882.  
 Méheust, Y., Fossum, J. O., Knudsen, K. D., Måløy, K. J. & Helgesen, G. (2006a). Mesosstructural changes in a clay intercalation compound during hydration transitions. Preprint.  
 Méheust, Y., Knudsen, K. & Fossum, J. O. (2006b). *J. Appl. Cryst.* **39**, 661–670.  
 Mourchid, A., Lecolier, E., van Damme, H. & Levitz, P. (1998). *Langmuir*, **14**, 4718–4723.  
 Pfeifer, P. & Avnir, D. (83). *J. Chem. Phys.* **79**, 3558–3565.  
 Porod, G. (1951). *Kolloid Z.*, **124**, 93–94.  
 Schaefer, D. W. & Keefer, K. D. (1986). *Phys. Rev. Lett.* **56**, 2199.  
 Schmidt, P. W. (1989). In *The fractal approach to heterogeneous chemistry*, edited by D. Avnir, pp. 67–79. John Wiley & Son Ltd.  
 da Silva, G. J., Fossum, J. O., Di Masi, E. & Måløy, K. (2003). *Phys. Rev. B*, **67**, 09411.  
 Sinha, S. K., Freltoft, T. & Kjems, J. K. (1984). In *Kinetics of Aggregation and Gelation*, edited by F. Family & D. P. Landau, pp. 87–90. Elsevier, Amsterdam.  
 Skipper, N. T., Refson, K. & McConnel, J. D. C. (1991). *J. Chem. Phys.* **94**(11), 7434.  
 Solin, S. A. (1993). In *Chemical Physics of Intercalation II*, edited by P. Bernier, J. E. Fischer, S. Roth & S. A. Solin, pp. 161–180. Plenum Press, New York.  
 Suzuki, M., Wada, N., Hines, D. R. & Whittingham, M. S. (1987). *Phys. Rev. B*, **36**(5), 2844–2851.  
 Vacher, R., Woignier, T., Pelous, J. & Courtens, E. (1988). *Phys. Rev. B*, **37**, 6500.  
 Velde, B. (1992). *Introduction to Clay Minerals*. Chapman and Hall.  
 Wada, N., Hines, D. R. & Ahrenkiel, S. P. (1990). *Phys. Rev. B*, **41**(18), 12895.

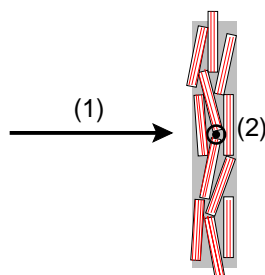


**Figure 1**  
 Sketch of a vertical cut of one  $2 \times 2 \times 6 \text{ mm}^3$  dry-pressed Na-fluorohectorite sample, as it stands in the beam. The gray shadings denote the sample's mesopores, while the red lines represent the nano-porosity inside the nano-stacks. Two configurations were used: one in which the beam is oriented with respect to the sample according to the direction denoted (1), and one in which it is oriented according to the direction denoted (2).

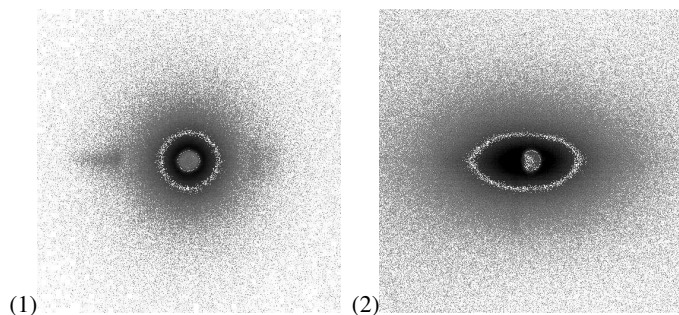


**Figure 2**  
 Two-dimensional SAXS images recorded in the two configurations (1) and (2) (see Fig. 1). In both images, a narrow range of intensities has been painted white so as to highlight the shape of an iso-intensity line: in (1), the image is isotropic; in (2), it is strongly anisotropic.

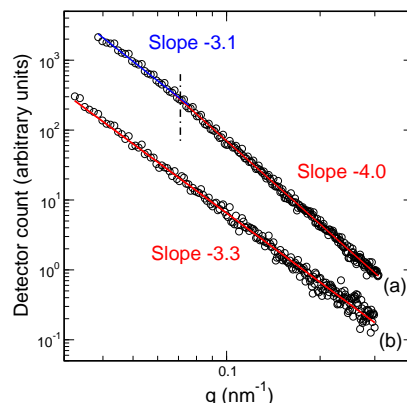


**Figure 3**  
 Radial intensity profiles from a SAXS image recorded at 393 K: (a) along the ellipse's long principal axis (close to horizontal in Fig. 2(2)), and (b) along the ellipse's short principal axis (close to vertical in Fig. 2(2)).

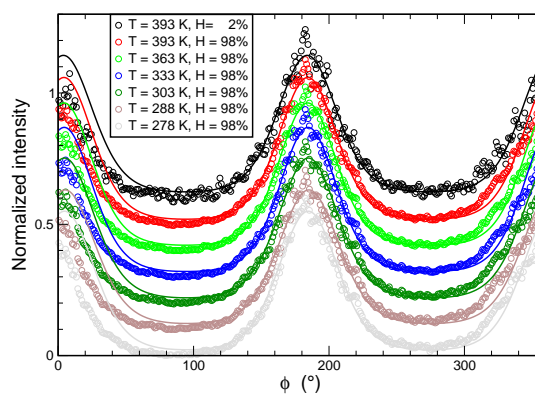


**Figure 4**  
 Azimuthal intensity profiles for a series of SAXS images recorded at decreasing temperature values. Maier-Saupe fits are superimposed to the data; they provide the ODP function for the nematic order of scattering objects in the sample.

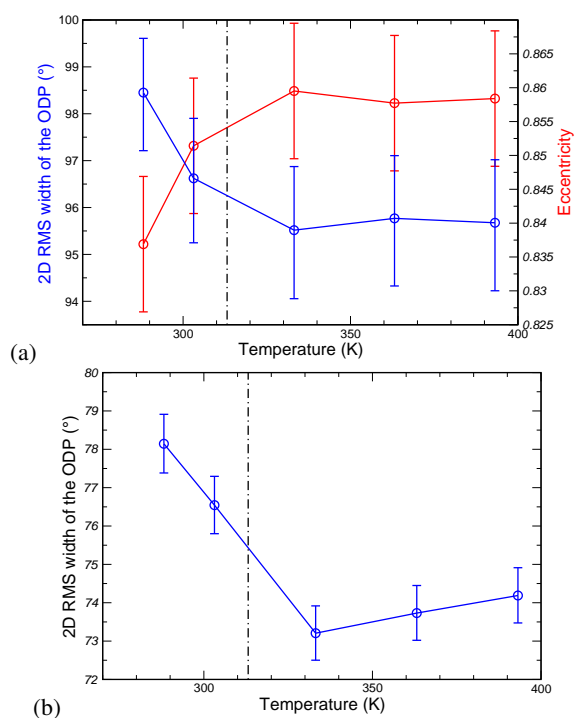


**Figure 5**  
 (a) Dependence on temperature of the eccentricity of iso-intensity lines (in red) and of the 2D RMS of the ODP functions (in blue) inferred from the eccentricity values. – (b) 2D RMS width of the ODP as directly obtained from the intensity profiles at a fixed  $q$  value (see Fig. 4). Both plots show that a moderate decrease of the orientational order occurs as particles swell by taking in one more layer of water, at around 313 K.